Multidimensional computations of a two-fluid hyperbolic model in a porous medium

Laëtitia Girault, Jean-Marc Hérard

Multidimensional computations of a two-fluid hyperbolic model in a porous medium

Laëtitia Girault †

† *EDF R&D, Fluid Dynamics, Power Generation and Environment, 6 quai Watier, 78400, Chatou, France, and: LATP, 39 rue Joliot Curie, 13453, Marseille cedex 13, France*

Jean-Marc Hérard⋆

⋆*EDF R&D, Fluid Dynamics, Power Generation and Environment, 6 quai Watier, 78400, Chatou, France.*

Jean-Marc.Herard@edf.fr

Abstract

This paper deals with the computation of two-phase flows in a porous medium, with two main objectives. First of all, we will present a new multi-dimensional well-balanced scheme, with its advantages and drawbacks. Furthermore, we will compare results of the porous model with approximations obtained with a full two-dimensional computation, where all obstacles have been taken into account in the computational domain. The two-phase flow model is hyperbolic, and the scheme takes its roots on a modified Rusanov scheme that integrates effects due to discontinuous porous profiles. The scheme perfectly maintains steady state profiles on any structured mesh.

Key words : Finite Volumes, Two-Fluid Model, Porous Medium

1 Introduction

We examine in this paper the numerical modelling of two-phase flows in a multidimensional computational domain that contains fluid and porous regions. The fluid region and the porous region are separated by a fixed coupling interface, which is assumed to be thin and plane. For clarity, we may imagine the following situation, with a plane with a given normal direction n, containing the point (x_0, y_0, z_0) ; the fluid and porous regions will respectively lie on the left and right sides of this fixed plane that will be called the coupling interface. Within both the fluid region and the porous region, a two-fluid model is considered in order to compute unsteady

flow patterns. Therefore, we will need to introduce -unsteady- boundary conditions on both sides of this sharp coupling interface, in such a way that waves travelling across this coupling interface do not introduce pollution in solutions of the coupled problem (we refer to [2, 11] which describe the general framework on the coupling of distinct fluid models). In the sequel, these boundary conditions at the coupling interface will sometimes be referred to as the coupling conditions. One of the main motivations for such a work in the framework of nuclear safety in power plants is that the meshing of some tiny obstacles cannot be afforded in many practical situations. This occurs for instance in the core of the nuclear reactor, but also in steam generators. The problem then is to provide some suitable model in order to take into account in a meaningful way porous regions and sharp free/porous interfaces.

As a first step, we shall assume given boundary conditions at the coupling interface (in a weak sense), and will focus on the way one should discretize governing equations, so that convergence towards exact solutions of the associated one-dimensional Riemann problem is retrieved when the mesh is refined. These exact solutions are of course tightly linked to the former -enforced- coupling conditions. More precisely, we will first detail the two-fluid hyperbolic model (2) that has been retained in order to compute approximations of solutions. This porous model issues from [16] , and has been examined in detail in this reference. We will only give here the main features that are needed for our purposes. The free version of this model identifies with models discussed in [1, 4, 7, 8, 9, 13, 19] . The coupling conditions that will be assumed here simply correspond to the preservation of Riemann invariants pertaining to the steady wave associated with system (2). We emphasize that this model is different from the one which is classically used in the nuclear industry (see for instance [22] and references therein), and also from those used in the oil industry [6] .

A presentation of the three-dimensional scheme will follow. We emphasize that the scheme relies in fact on Greenberg and Leroux ideas (see [12]), which have been recently revisited by Kröner and Thanh (see [21, 20]). The main idea is to integrate in the well-balanced scheme an interface flux that is easier -and cheaper- to compute than the original interface Godunov state, as it was first proposed by authors of [12] . This interface flux should nonetheless be "clever enough", in order to guarantee that steady states are perfectly preserved whatever the mesh size. As it was first reported in [10] to our knowledge, the preservation of well-balanced initial conditions by the scheme seems mandatory ; otherwise, convergence towards wrong solutions is observed when the mesh size h tends to 0. The main properties of the simple well-balanced scheme will be given.

Numerical results will be provided in the last section. We recall that convergence studies have been performed in the one-dimensional framework in the companion work [10] . Emphasis will thus be given on multi-dimensional computations. Actually, we will discuss a comparison that has been performed between two numerical experiments on *different* meshes. The first experiment corresponds to the computation of the true geometry including obstacles in the computational domain. In the second one, the region including obstacles is assumed to be a porous region. The

influence of the topology of the region filled with obstacles and also of the mesh size are examined in this section devoted to numerical results. This enables us to draw some conclusions and perspectives for future work.

2 Governing equations of the two-fluid model

We start by recalling the governing equations of the two-fluid two-pressure model that we use for computations of two-phase flows in a porous medium. (see [16] for a brief introduction). As usual, we define the void fraction $\alpha_k \in [0,1]$ (such that $\alpha_1 + \alpha_2 = 1$), the porosity $\epsilon \in]0,1]$, the mean velocity U_k, the mean pressure P_k, the mean density ρ_k, and the internal energy $e_k(P_k, \rho_k)$ in phase k, for $k = 1, 2$. The state variable W in $\mathbf{R}^{12}$ is:

$$W^t = (\epsilon, \alpha_2, \epsilon m_1, \epsilon m_2, \epsilon m_1 U_1^t, \epsilon m_2 U_2^t, \epsilon\alpha_1 E_1, \epsilon\alpha_2 E_2) \tag{1}$$

that will be noted in a short way : $W^t = (\epsilon, \alpha_2, \epsilon m_k, \epsilon m_k U_k^t, \epsilon\alpha_k E_k)$ in the following. We will also note $m_k = \alpha_k\rho_k$ the partial mass in phase k, and $E_k = \rho_k||U_k||^2/2 + \rho_k e_k(P_k, \rho_k)$ the total energy of phase k. T_k denotes the temperature of phase k.

The two-fluid model reads:

$$\begin{cases} \partial_t(\epsilon) = 0 \\ \partial_t(\alpha_2) + V_I.\nabla(\alpha_2) = \phi_2(W) \\ \partial_t(\epsilon m_k) + \nabla.(\epsilon m_k U_k) = 0 \\ \partial_t(\epsilon m_k U_k) + \nabla.(\epsilon m_k U_k \otimes U_k) + \epsilon\alpha_k\nabla(P_k) + \epsilon(P_k - P_I)\nabla(\alpha_k) = \epsilon D_k(W) \\ \partial_t(\epsilon\alpha_k E_k) + \nabla.(\epsilon\alpha_k U_k(E_k + P_k)) + \epsilon P_I\partial_t(\alpha_k) = \epsilon\psi_k + \epsilon V_I.D_k(W)\ . \end{cases} \tag{2}$$

The contribution D_k refers to the drag forces, and the contributions ϕ_k and ψ_k respectively correspond to the return to a pressure/thermal equilibrium. Mass transfer might be included in equations (2), but it will not be considered herein.

The closure laws for the source terms (ϕ_2, D_k, ψ_k) are the following:

$$\sum_{k=1}^{2} D_k(W) = 0 \quad ; \quad \sum_{k=1}^{2} \psi_k(W) = 0\ . \tag{3}$$

where:

$$\begin{cases} D_k = (-1)^k \frac{m_1 m_2}{(m_1+m_2)}(U_1 - U_2)/\tau_U \\ \phi_2 = \frac{\alpha_1\alpha_2}{|P_1|+|P_2|}(P_2 - P_1)/\tau_P \\ \psi_k = K_T(1/T_k - 1/T_{3-k}) \end{cases} \tag{4}$$

where τ_U and τ_P denote relaxation time scales (assuming that $0 < \tau_P < \tau_U$), while K_T is positive. We also need to define specific entropies. If we set :

$$(c_k(P_k, \rho_k))^2 = \left(\frac{P_k}{(\rho_k)^2} - \partial_{\rho_k}(e_k(P_k, \rho_k))\right)(\partial_{P_k}(e_k(P_k, \rho_k)))^{-1} \tag{5}$$

the specific phasic entropy $s_k(P_k, \rho_k)$ complies with:

$$(c_k(P_k, \rho_k))^2 \partial_{P_k} (s_k(P_k, \rho_k)) + \partial_{\rho_k} (s_k(P_k, \rho_k)) = 0 \tag{6}$$

For liquid-vapour applications, where the vapour phase is assumed to be dilute, a meaningful couple for the interfacial velocity and the interfacial pressure is :

$$(V_I, P_I) = (U_2, P_1)$$

(see [4, 7, 9, 19]). The index 2 refers to the vapour phase. As recalled in the following section, the specific choice $(V_I, P_I) = (U_2, P_1)$ has a great impact on properties of the system of PDE that governs the motion of the fluids.

Though we do not consider them here, we emphasize that friction effects inside the porous medium may be taken into account in a classical way, and also that this does not modify the main properties of the whole model that are discussed below (see appendix B).

3 Main properties

We recall here that :

- the nonhomogeneous system (2) is hyperbolic;
- smooth solutions of (2) comply with a physically relevant entropy inequality;
- system (2) admits unique jump conditions within each isolated genuinely nonlinear (GNL) field (see appendix C).

If we focus on the convective part -left hand side- of (2), we can first rewrite (2) in a non-conservative form as follows:

$$\partial_t (W) + A_x(W)\partial_x (W) + A_y(W)\partial_y (W) + A_z(W)\partial_z (W) = 0 \tag{7}$$

Thus, if we define the unit vector $n = (n_x, n_y, n_z)$, we may introduce $A(W, n)$ as:

$$A(W, n) = n_x A_x(W) + n_y A_y(W) + n_z A_z(W) \tag{8}$$

Hence we get:

Proposition 1a :
The matrix $A(W, n)$ admits the following real eigenvalues:

$$\begin{array}{l} \lambda_0 = 0 \quad , \quad \lambda_1 = V_I \cdot n, \\ \lambda_{2-4} = U_1 \cdot n \quad , \quad \lambda_5 = U_1 \cdot n - c_1 \quad , \quad \lambda_6 = U_1 \cdot n + c_1, \\ \lambda_{7-9} = U_2 \cdot n \quad , \quad \lambda_{10} = U_2 \cdot n - c_2 \quad , \quad \lambda_{11} = U_2 \cdot n + c_2 \end{array} \tag{9}$$

We may now define a frame change introducing τ_1 and τ_2 such that (n, τ_1, τ_2) defines a fixed orthonormal basis. Taking into account the invariance under frame

rotation of equations (2), and neglecting transverse derivatives of all components, thus setting:

$$\partial_{x_{\tau_k}}(\phi) = 0$$

for $k = 1, 2$, whatever ϕ is, we focus now on the corresponding one-dimensional problem in the n direction associated with :

$$\begin{cases} \partial_t(\epsilon) = 0 \\ \partial_t(\alpha_2) + (V_I \cdot n)\partial_{x_n}(\alpha_2) = 0 \\ \partial_t(\epsilon m_k) + \partial_{x_n}(\epsilon m_k (U_k \cdot n)) = 0 \\ \partial_t(\epsilon m_k U_k \cdot n) + \partial_{x_n}\left(\epsilon m_k (U_k \cdot n)^2\right) + \epsilon\alpha_k \partial_{x_n}(P_k) + \epsilon(P_k - P_I)\partial_{x_n}(\alpha_2) = 0 \\ \partial_t(\epsilon\alpha_k E_k) + \partial_{x_n}(\epsilon\alpha_k (U_k \cdot n)(E_k + P_k)) + \epsilon P_I \partial_t(\alpha_k) = 0 \\ \partial_t(\epsilon m_k (U_k \cdot \tau_1)) + \partial_{x_n}(\epsilon m_k (U_k \cdot n)(U_k \cdot \tau_1)) = 0 \\ \partial_t(\epsilon m_k (U_k \cdot \tau_2)) + \partial_{x_n}(\epsilon m_k (U_k \cdot n)(U_k \cdot \tau_2)) = 0 \ . \end{cases} \tag{10}$$

A straightforward analysis of (10) provides the following result:

Proposition 1b :
System (10) *admits real eigenvalues detailed in* (9)*. Associated right eigenvectors span the whole space if :* $|(V_I - U_k) \cdot n| \neq c_k$*, and* $|U_k \cdot n| \neq c_k$*, for* $k = 1, 2$*.*

Waves associated with eigenvalues $\lambda_0, \lambda_{2-4}, \lambda_{7-9}$ *are linearly degenerate. If we assume that* $V_I = U_k$*, or* $V_I = (m_1 U_1 + m_2 U_2)/(m_1 + m_2)$*, the wave associated with the eigenvalue* $\lambda_1 = V_I \cdot n$ *is linearly degenerate. The other waves associated with* $\lambda_5, \lambda_6, \lambda_{10}, \lambda_{11}$ *are genuinely non-linear.*

The proof is simple, and we refer to [7, 9] for similar results in a non-porous framework, and also to [16] in a one-dimensional framework. The specific choice for V_I is extremely important since it guarantees well-posed jump conditions through single shock waves.

Moreover, if we define the entropy-entropy flux : (η, f_η) as follows:

$$\eta = \epsilon(m_1 \ln(s_1) + m_2 \ln(s_2))$$

$$f_\eta = \epsilon(m_1 \ln(s_1) U_1 + m_2 \ln(s_2) U_2)$$

and introduce the corresponding source term :

$$S_\eta(W) = \epsilon \sum_{k=1,2} \Big(m_k(\psi_k - D_k(U_k - V_I) + (-1)^k \phi_2(P_I - P_k))/T_k \Big)$$

we get the next result:

Proposition 2 :
The following entropy inequality holds for smooth solutions of system (2)*:*

$$\partial_t(\eta) + \nabla.(f_\eta) = S_\eta(W) \geq 0 \ . \tag{11}$$

This also is a direct consequence of the definition of the couple (V_I, P_I) given above. For shock solutions travelling at speed σ in the n direction, and seperating two states W_l, W_r, the entropy inequality is :

$$-\sigma(\eta(W_r) - \eta(W_l)) + (f_\eta(W_r) - f_\eta(W_l)) \cdot n > 0 \ . \tag{12}$$

Eventually, we need to detail the structure of the standing wave, which corresponds to a LD wave. Actually, the following Riemann invariants will be the keystone for the definition of the simple well-balanced scheme that will be introduced hereafter.

Proposition 3 :
We focus on the one-dimensional Riemann problem associated with (10)*. The linearly degenerate (LD) wave associated with $\lambda_0(W)$ admits the following Riemann invariants*

$$\begin{array}{l} I_1^0(W) = \alpha_2 \quad ; \quad I_2^0(W) = s_1 \quad ; \quad I_3^0(W) = \epsilon m_1 U_1 \cdot n \\ I_4^0(W) = e_1 + \frac{P_1}{\rho_1} + \frac{||U_1||^2}{2} \quad ; \quad I_5^0(W) = s_2 \\ I_6^0(W) = \epsilon m_2 U_2 \cdot n \quad ; \quad I_7^0(W) = e_2 + \frac{P_2}{\rho_2} + \frac{||U_2||^2}{2} \\ I_8^0(W) = U_1 \cdot \tau_1 \quad ; \quad I_9^0(W) = U_1 \cdot \tau_2 \\ I_{10}^0(W) = U_2 \cdot \tau_1 \quad ; \quad I_{11}^0(W) = U_2 \cdot \tau_2 \end{array}$$

The proof is straightforward. Assuming that $r_0(W)$ denotes the right eigenvector associated with $\lambda_0(W)$, it only requires to check that $\nabla_W I_k^0(W) \cdot r_0(W) = 0$, for $k = 1, ..., 11$.

4 A simple well-balanced Finite Volume scheme

We describe herein the simple well-balanced Finite Volume scheme we use. This one is grounded on basic ideas of well-balanced schemes introduced by Greenberg and Leroux (see [12]). Within each Finite Volume ω_i of size Ω_i, an approximation of the mean value of W at time t^n in cell i is:

$$W_i^n \simeq (\int_{\omega_i} W(x, t^n) dx) / \int_{\omega_i} dx \tag{13}$$

The time step Δt^n will be defined later on (see Proposition 5). Moreover, we define:

$$\overline{a}_{ij} = (a_i + a_j)/2$$

where i, j refer to indexes of two neighbouring cells. S_{ij} denotes the surface of the interface connecting cells i and j.

We define the state variable $Z^t = (\alpha_2, m_k, m_k U_k, \alpha_k E_k)$ in $\mathbf{R}^{11}$. Given some unit normal vector n, we define the normal flux $f_n(Z, n)$ in $\mathbf{R}^{11}$ as follows:

$$f_n(Z, n)^t = (0, m_k U_k \cdot n, (m_k U_k \cdot n) U_k + \alpha_k P_k n, \alpha_k U_k \cdot n (E_k + P_k)) \tag{14}$$

We use a splitting technique in order to discretize convective terms and source terms. In step I, we compute explicit approximations of solutions of the homogeneous problem associated with the left-hand side of (2). Then source terms are taken into account in step II using implicit schemes. Actually, the computation of the whole set (2) complies with the overall entropy inequality (11).

The first step thus reads :

$$\left\{\begin{array}{l} \partial_t(\epsilon) = 0 \\ \partial_t(\alpha_2) + V_I \cdot \nabla(\alpha_2) = 0 \\ \partial_t(\epsilon m_k) + \nabla \cdot (\epsilon m_k U_k) = 0 \\ \partial_t(\epsilon m_k U_k) + \nabla \cdot (\epsilon m_k U_k \otimes U_k) + \epsilon \alpha_k \nabla(P_k) + \epsilon(P_k - P_I)\nabla(\alpha_k) = 0 \\ \partial_t(\epsilon \alpha_k E_k) + \nabla \cdot (\epsilon \alpha_k U_k (E_k + P_k)) + \epsilon P_I \partial_t(\alpha_k) = 0 \ . \end{array}\right. \tag{15}$$

Numerical algorithms that are needed to compute approximations of solutions of the ODE (16) in the second step:

$$\left\{\begin{array}{l} \partial_t(\epsilon) = 0 \\ \partial_t(\alpha_2) = \phi_2(W) \\ \partial_t(\epsilon m_k) = 0 \\ \partial_t(\epsilon m_k U_k) = \epsilon D_k(W) \\ \partial_t(\epsilon \alpha_k E_k) + \epsilon P_I \partial_t(\alpha_k) = \epsilon \psi_k + \epsilon V_I . D_k(W) \ . \end{array}\right. \tag{16}$$

or alternatively :

$$\left\{\begin{array}{l} \partial_t(\epsilon) = 0 \\ \partial_t(\alpha_2) = \phi_2(W) \\ \partial_t(m_k) = 0 \\ \partial_t(m_k U_k) = D_k(W) \\ \partial_t(\alpha_k E_k) + P_I \partial_t(\alpha_k) = \psi_k + V_I . D_k(W) \ . \end{array}\right. \tag{17}$$

are detailed in [9, 17] and thus are not recalled here.

The discrete variable ϵ is assumed to be constant within each cell. The cell scheme is:

$$\Omega_i(Z_i^{n+1} - Z_i^n) + \Delta t^n \sum_{j \in V(i)} \Big(F(Z_i^n, Z_{ij,i}^n, n_{ij}) S_{ij} \Big) + \Delta t^n (NCT)_i^n = 0 \tag{18}$$

$V(i)$ contains all neighbouring cells of cell i, and n_{ij} is the outward normal vector pointing from cell i to cell$j$.

The numerical flux is defined by:

$$F(Z_i^n, Z_{ij,i}^n, n_{ij}) = \big(f_n(Z_i^n, n_{ij}) + f_n(Z_{ij,i}^n, n_{ij}) - (r_{WB})_{ij}^n (Z_{ij,i}^n - Z_i^n) \big)/2 \tag{19}$$

where the scalar $(r_{WB})_{ij}^n$ is defined as:

$$(r_{WB})_{ij}^n \stackrel{def}{=} \max_{k=1,2} (|(U_k \cdot n)_{ij,i}^n|, |(U_k \cdot n)_{ij,j}^n|, r_i^n, r_j^n)$$

where r_i^n stands for the spectral radius of the Jacobian matrix $A(W_i^n, n)$ introduced in (8).

The contribution of non-conservative terms $(NCT)_i^n$ is a rough centered approximation as follows:

$$NCT_i^n = ...$$
$$\left((V_I)_i^n \cdot \sum_{j \in V(i)} (\overline{\alpha}_2)_{ij} n_{ij} S_{ij}, 0, -(P_I)_i^n \sum_{j \in V(i)} (\overline{\alpha}_k)_{ij} n_{ij} S_{ij}, -(P_I)_i^n (V_I)_i^n \cdot \sum_{j \in V(i)} (\overline{\alpha}_k)_{ij} n_{ij} S_{ij} \right) \tag{20}$$

This centered scheme is admissible since the diffusion coefficient $(r_{WB})_{ij}^n$ in the flux definition takes all wave speeds of the whole convective set into account.

The values $Z_{ij,i}^n$ are obtained by solving the non-linear equations (for $m = 0$ to 10):

$$Inv_m^0(Z_{ij,i}^n, \epsilon_i) = Inv_m^0(Z_j^n, \epsilon_j) \tag{21}$$

Quantities $Inv_m^0(Z, \epsilon)$ are straightforward extensions of the eleven Riemann invariants of the standing wave introduced in Proposition 3. Thus we have:

$$\begin{array}{l} Inv_0^0(Z, \epsilon) = \alpha_2 \\ Inv_{5k-4}^0(Z, \epsilon) = s_k(P_k, \rho_k) \\ Inv_{5k-3}^0(Z, \epsilon) = \epsilon m_k U_k \cdot n \\ Inv_{5k-2}^0(Z, \epsilon) = U_k \cdot \tau_1 \\ Inv_{5k-1}^0(Z, \epsilon) = U_k \cdot \tau_2 \\ Inv_{5k}^0(Z, \epsilon) = e_k(P_k, \rho_k) + P_k/\rho_k + ||U_k||^2/2 \end{array} \tag{22}$$

for $k = 1, 2$. If $\epsilon_i = \epsilon_j$, then obviously $Z_{ij,i}^n = Z_j^n$ is a solution. Moreover, we also get in that case : $Z_{ij,j}^n = Z_i^n$, and thus the normal flux is continuous through the interface ij. A straightforward consequence is that, if NCT is null (assuming a constant void fraction), one retrieves the conservative form of equations when the porosity is locally uniform. In addition, the scheme identifies with the classical Rusanov scheme in that case. We must note here that the last Riemann invariant $Inv_{5k}^0(Z, \epsilon)$ may be written in a slightly different form, since:

$$Inv_{5k}^0(Z, \epsilon) = e_k(P_k, \rho_k) + P_k/\rho_k + (U_k \cdot n)^2/2 + (Inv_{5k-1}^0(Z, \epsilon)^2 + Inv_{5k-2}^0(Z, \epsilon)^2)/2 \tag{23}$$

which means that the quantity $e_k(P_k, \rho_k) + P_k/\rho_k + (U_k \cdot n)^2/2$ should be preserved, and this is exactly equivalent to the one-dimensional formulation (see [10]). Details pertaining to the exact computation of the quantities $Z_{ij,i}^n$ are given in appendix D. In practice, this step requires solving two uncoupled non-linear scalar equations on both sides of the cell interface ij, for both phases. More precisely, we need to compute four quantities $(\rho_k)_{ij,i}^n$ and $(\rho_k)_{ij,j}^n$ (for $k = 1, 2$) at each cell interface ij. Each non-linear scalar equation involves a function $\psi(X)$ which is either increasing with respect to X, or decreasing and then increasing (which is the general case). Thus the computation of solutions is rather easy and it is not consuming too much CPU time. We give now the main properties of the scheme.

5 Main properties of the scheme

In the framework of one-dimensional computations, this simple well-balanced scheme preserves flows at rest, even when the porosity is not uniform (see [10]). Turning then to multi-dimensional flows, and assuming some restrictions on the EOS, one may check that some basic contact solutions of the form :

$$P_k(.,t) = P_0 \qquad U_k(.,t) = U_0 \qquad V_k(.,t) = W_k(.,t) = 0$$

are perfectly predicted on *any* structured rectangular mesh, when restricting to uniform porous profiles (the proof is obvious and similar to the one given in [10] in the pure one-dimensional framework).

Moreover, based on [10] , it seems in practice that the well-balanced property is necessary in order to obtain convergence towards the correct one-dimensional discontinuous solutions, when the initial data contains discontinuous values of porosity. Thus the following result is indeed crucial:

- *Proposition 4:*
  We consider initial data for a one-dimensional Riemann problem, such that $\epsilon_L \neq \epsilon_R$. *We assume that the initial conditions* (W_L, W_R) *of the Riemann problem comply with :* $I_m^0(W_L) = I_m^0(W_R)$, *for* $m = 1$ *to* 11. *Then the scheme (*(18),(21)*) introduced in the previous section preserves steady states on any structured mesh.*

  A crucial point in the proof is linked with the exact computation of the $Z_{ij,i}$. The proof is almost the same as the one given in [10] . We must recall here that more classical schemes (such as Rusanov scheme for instance) do not ss enjoy this latter property, and it has been pointed out in [10] that a straighforward consequence is that these schemes do not guarantee convergence towards the right solutions, when sharp discontinuities on ϵ are present in the computational domain.

  Eventually, the next result provides a useful condition on the time step Δt^n :

- *Proposition 5:*
  Both void fractions α_1 *and* α_2 *and partial masses* m_1, m_2 *remain positive provided that the following CFL condition holds:*

$$\frac{\Delta t^n}{2\Omega_i} \sum_{j \in V(i)} (r_{WB})_{ij}^n S_{ij} \leq 1 \qquad \forall i \tag{24}$$

The proof is given in appendix A.

6 Numerical results

In this section, we will first examine some one-dimensional tests in order to validate the algorithms. Afterwards, we will focus on a comparison between two different approaches. In a first series of tests, we will compute the fluid flow in a channel with a pure free medium at the inlet, followed by a sudden uniform porous region. Then, we will examine the true behaviour of the fluid when the computational domain takes obstacles into account, and thus requires no homogeneization. Hence the main objective in the second part is to examine the suitability of the coupling conditions between free and porous media. The well-balanced formalism that has been implicitly retained in the formulation of coupling boundary conditions enforces the continuity of Riemann invariants of the steady wave (see Proposition 3). Actually, we may expect that the conservation of both mass flux and total enthalpy holds through the counterpart of the sharp free/porous interface, when focusing on the true multidimensional simulation including an accurate description of obstacles. However, on the other hand, the preservation of the entropy seems questionable. Thus we will focus on three specific variables when comparing numerical results, which are : $\epsilon m_k U_k \cdot n$, s_k, and the total enthalpy H_k defined as:

$$H_k = (E_k + P_k)/\rho_k$$

All numerical experiments have been achieved using perfect gas EOS, setting $\gamma_1 = 1.1$ and $\gamma_2 = 1.4$.

6.1 Some one-dimensional test cases

Initial values of velocity components in y, z directions have been set to 0 in the following two test cases, and regular cubic meshes have been used.

6.1.1 Analytical test cases

- We start with a one-dimensional test case where initial conditions are well-balanced. In practice, we consider the following values:

	state L	state R
γ_1	1.1	
γ_1	1.4	
ϵ	1	0.6
α_1	0.95	
ρ_1	1000	
U_1	0	
P_1	100000	
ρ_2	100	92.0641467
U_2	10	18.1033195
P_2	100000	89069.0346

  The computational domain is $[0, 1]$. The initial discontinuity is located at $x = 0.5$, and the CFL number has been set to $1/2$. We use a coarse mesh

with 100 regular cells in order to emphasize differences between the present well-balanced scheme WBR which complies with Proposition 4, and the classical Rusanov scheme. We have plotted the three Riemann invariants $\epsilon m_k U_k$, S_k and H_k for both phases (see Figure 1), and also the three main variables ρ_k, U_k, P_k (see Figure 2). We can observe spurious oscillations due to the coupling interface when focusing on Rusanov scheme, whereas the well-balanced scheme performs perfectly well and maintains initial data steady. This was expected of course, owing to Proposition 4 given above. The exact solution and the WBR approximation are identical in this case. We insist that a mesh refinement does not yield convergence towards the correct solution when restricting to Rusanov scheme, which cannot be guessed when looking at results below.

- The second test is a Riemann problem for which an exact solution is available. This test case, that has been introduced in [10] , corresponds to a one-dimensional Riemann problem. It involves many "ghost" waves in the x-direction, through which no variation of the state variable occurs. The computational domain is still $[0, 1]$, and the initial discontinuity is again located at $x = 0.5$. The mesh contains 5000 cubic cells and the CFL number is set to $1/2$. Intermediate states only vary through the waves associated with eigenvalues $\lambda_0 = 0$, $\lambda_1 = U_2 = V_i$ and $\lambda_{11} = U_2 + c_2$. Initial conditions for left and right states W_L and W_R are recalled below, together with values of the two -non trivial- intermediate states W_A and W_B.

	state L	state A	state B	state R
ϵ	1	0.6		
α_1	0.95		0.05	
ρ_1	1	0.999190167	0.853058301	
U_1	10	16.6801748	-160.919041	
P_1	100000	99910.922	83960.8032	
ρ_2	0.1	0.0998565629	0.15	0.1
U_2	15	25.0359108		-346.262753
P_2	10000	9979.92457	94534.4211	53175.6119

Setting $\xi = (x - 1/2)/t$, the analytic solution is :

$$\begin{cases} W(\xi) = W_L & \text{when:} \quad \xi < 0 \\ W(\xi) = W_A & \text{when:} \quad 0 < \xi < U_I \\ W(\xi) = W_B & \text{when:} \quad U_I < \xi < \sigma_2 \\ W(\xi) = W_R & \text{when:} \quad \sigma_2 < \xi \end{cases} \tag{25}$$

where $U_I = (U_2)_A = (U_2)_B$ and $\sigma_2 = [\rho_2 U_2]_B^R / [\rho_2]_B^R$. Figure 3 shows the behaviour of both pressures P_1, P_2 and velocities U_1, U_2. Due to the numerical viscosity of scheme WBR, we can hardly distinguish states $(P_2)_A$ and $(P_2)_L$. This is emphasized by the fact that these two values are close to one another, and it is also due to the slow velocity of the void fraction wave V_I compared

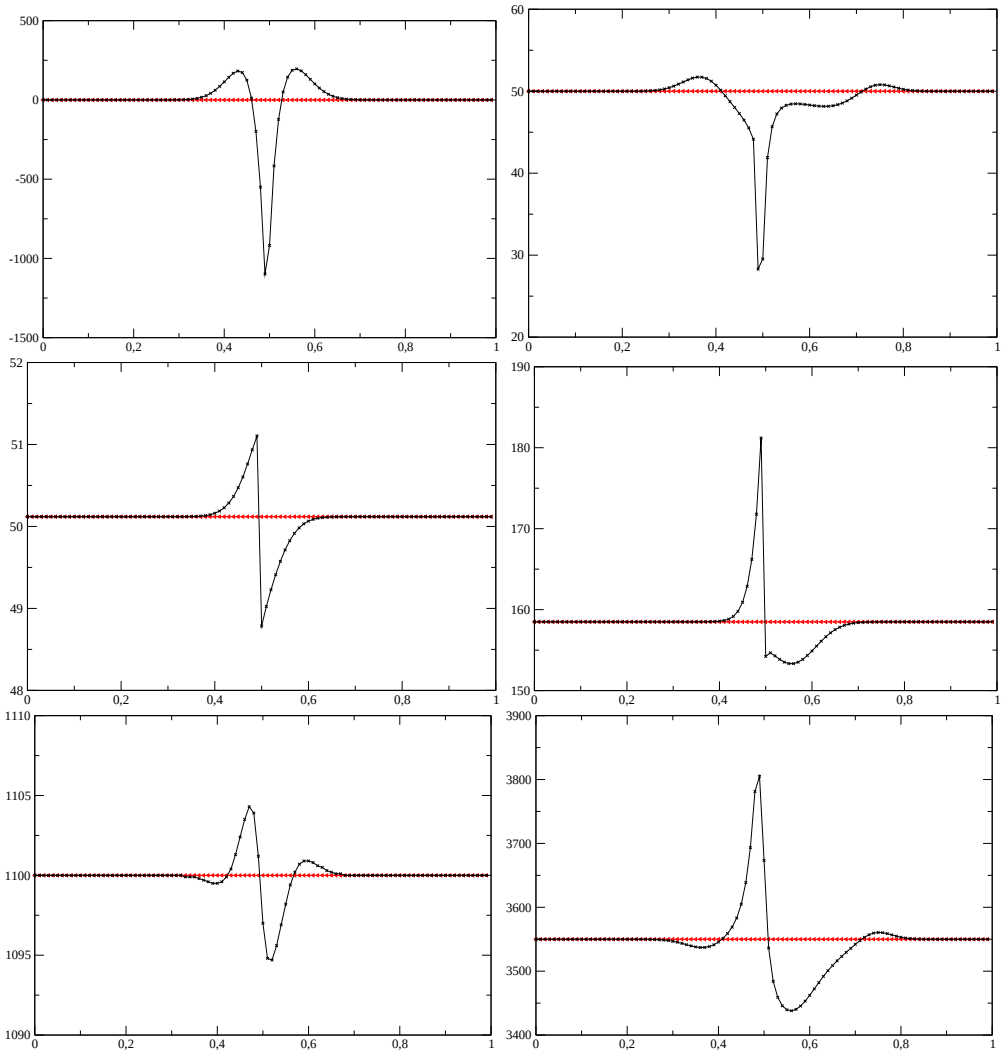

Figure 1: Riemann invariants of the steady wave for the well-balanced test case. The red line with triangles corresponds to scheme WBR, and the dark line with crosses corresponds to Rusanov approximation. Mean discharges Q_1 (left) and Q_2 (right) -top- Entropies S_1 (left) and S_2 (right) -middle- Total enthalpies H_1 (left) and H_2 (right) -bottom-

with the speed of the $2-$shock. No spurious behaviour is observed through the two LD waves associated with λ_0 and $\lambda_1 = V_I$.

These results are exactly the same as those obtained with the pure 1D algorithm. We retrieve the expected $h^{1/2}$ convergence towards the exact solution, for fine enough meshes (see [10]).

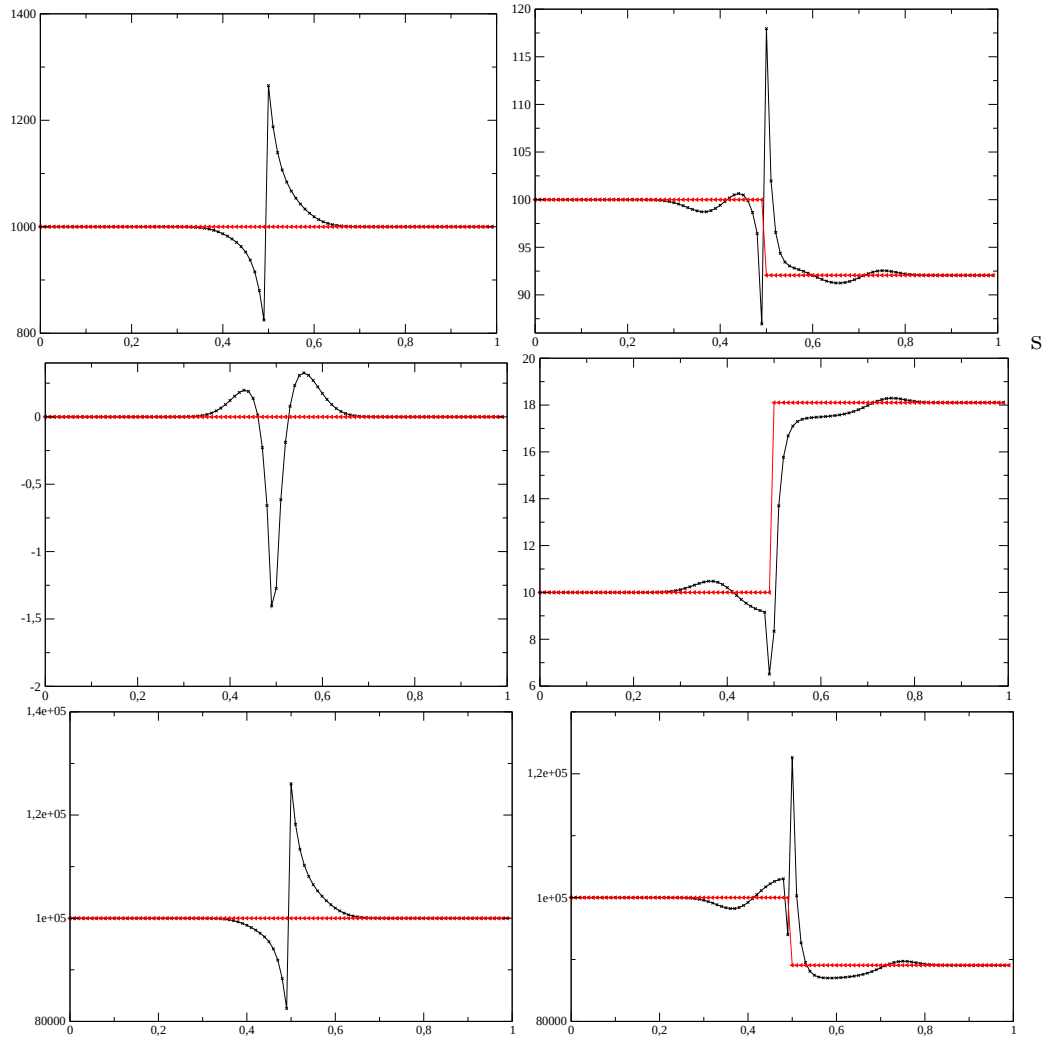

Figure 2: Variables ρ_k, U_k, P_k in the well-balanced test case, respectively on top, middle, bottom. The red line with triangles corresponds to scheme WBR, and the dark line with crosses corresponds to Rusanov approximation. Mean densities ρ_1 (left) and ρ_2 (right) -top- Velocities U_1 (left) and U_2 (right) -middle- Pressures P_1 (left) and P_2 (right) -bottom-

6.1.2 Propagation of a strong shock wave in a one-dimensional duct

This second test is also the exact counterpart of another test case investigated in [10] . A right-going shock wave is generated at $x_r = 0.65$ in the x-direction, on the left side of a sharp free/porous interface located at $x_p = 0.67$. The porosity profile is $\epsilon(x, y, z) = 1$ for $x < x_p$ and $\epsilon(x, y, z) = 0.6$ for $x > x_p$. We have set here $CFL = 1/2$, and the mesh contains 1000 regular cubic cells. Initial states on both sides of x_r are :

$$(\alpha_2)_L = 0.95 \quad (P_1)_L = (P_2)_L = 10^6 \quad (U_1)_L = (U_2)_L = 0 \quad (\rho_1)_L = 1 \quad (\rho_2)_L = 20$$

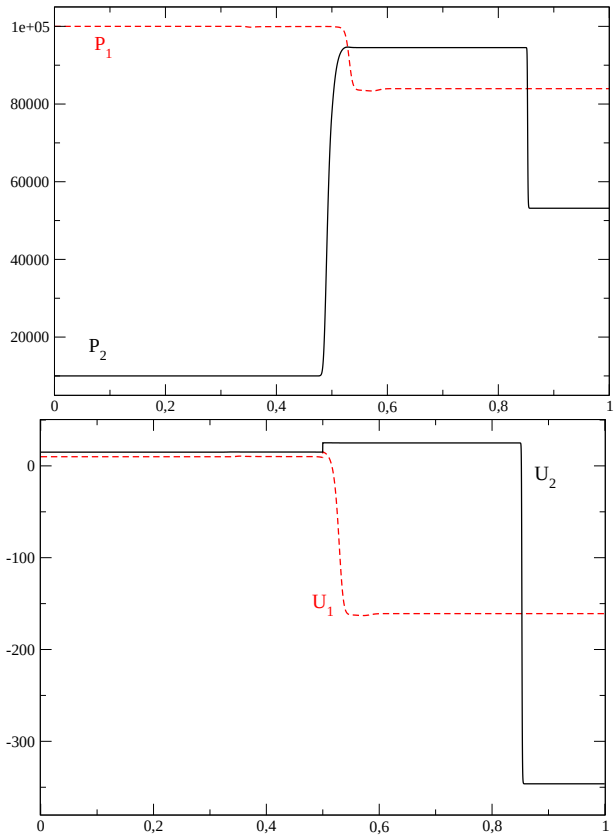

Figure 3: Pressure and velocity profiles along the x-axis of the duct for test case 1.

and :

$$(\alpha_2)_R = 0.05 \quad (P_1)_R = (P_2)_R = 10^5 \quad (U_1)_R = (U_2)_R = 0 \quad (\rho_1)_R = 1 \quad (\rho_2)_R = 20$$

In Figure 4, the solution has been plotted along the x-axis when the initial right-going shock wave is close to the right exit boundary. It may be checked that both Riemann invariants of the steady wave H_k and s_k remain uniform across the free/porous interface $x_p = 0.67$.

6.1.3 Comments

The computational results that have been obtained for these two test cases in the x-direction are exactly the same as the pure 1D results discussed in [10] . Moreover, we emphasize that the same test cases in y direction (respectively in z direction) have been computed, and provide exactly the same results.

We focus now on multidimensional computations in order to evaluate the porous approach that has been proposed before.

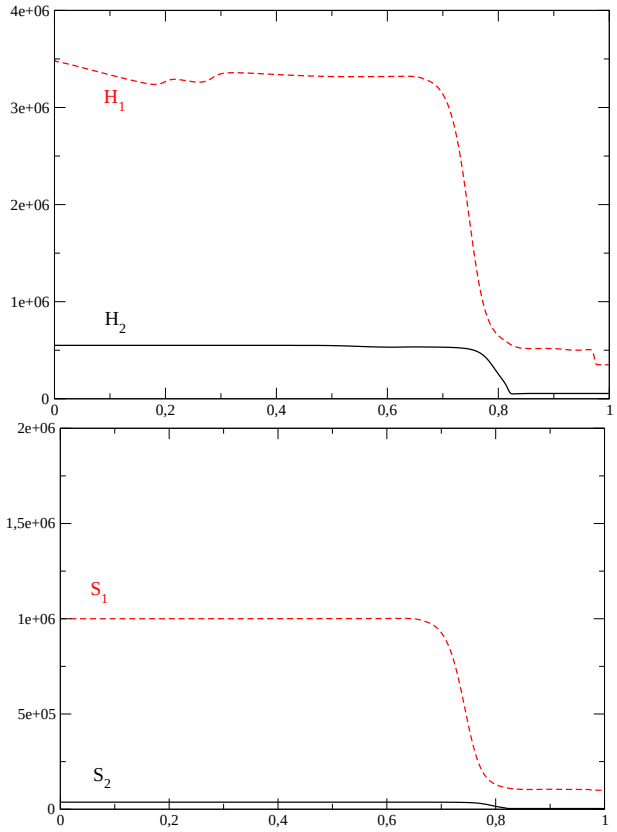

Figure 4: Enthalpy profiles H_1, H_2 -top- and entropy profiles S_1, S_2 -bottom- along the x-axis of the duct for test case 2.

6.2 Comparing the free and the porous approaches

6.2.1 Test 3: Transition between a free medium and a porous medium

In order to compare the porous and free approaches, we compute the free flow in a rectangular computational domain $[0, 24] \times [0, 40]$ containing six identical rectangular obstacles aligned with the y-direction on the upper part of the domain (for $y \in [20, 40]$). Within this region, the fluid can flow through a surface, the aspect ratio of which is $1/2$. A sketch is given in Figure 5 with different meshes.

In a second experiment, we consider the porous approach proposed in the first section. Thus, the computational domain is now the full rectangle $(x, y) \in [0, 24] \times [0, 40]$. The porosity distribution is given by $\epsilon(x, y) = 1$, except for the upper region where $\epsilon(x, y) = 1/2$, for $y \in [20, 40]$. A very coarse mesh has been used here first (960 square cells), since it corresponds to the real mesh size that one can afford in practice for industrial computations.

The same inlet (for $y = 0$) boundary conditions are used for the free and the porous approach, and inlet states are : $P_1 = P_2 = 10^5$, $V_1 = V_2 = 100$, $\alpha_1 = 0.95$ and $\rho_1 = 1$, $\rho_2 = 1$. Homogeneous Neumann outlet (for $y = 40$) boundary conditions

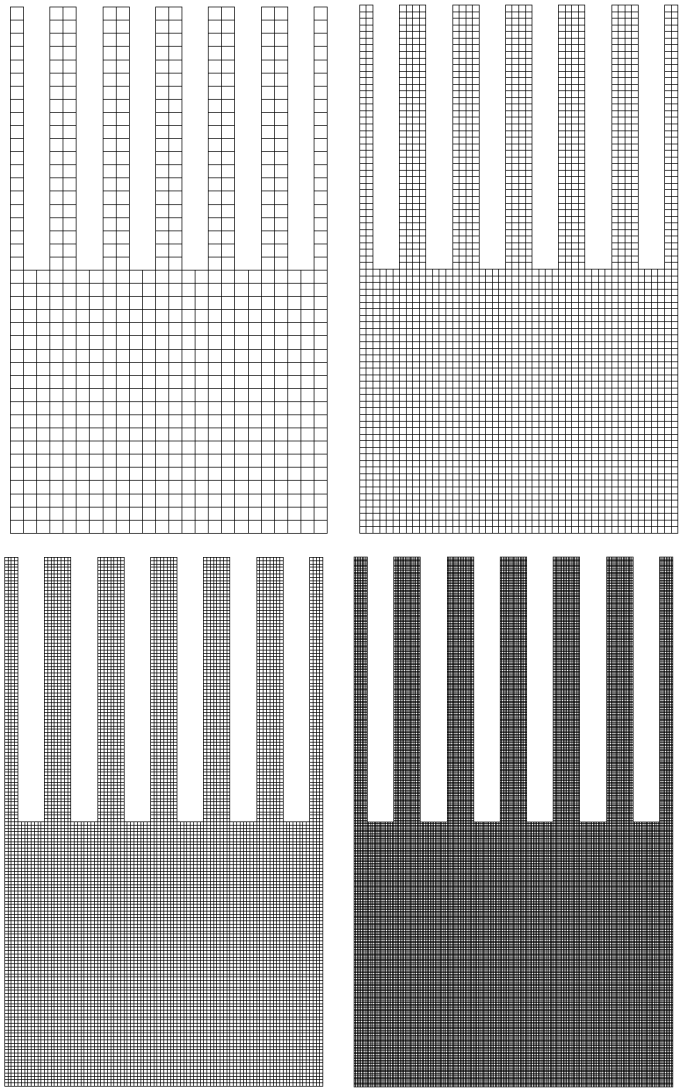

Figure 5: Computational domains used for the free approach with six identical rectangular obstacles in Test 3 (with one medium change). Top : 24 cells on X, 40 on Y (left) , 48 cells on X, 80 on Y (right). Bottom: 96 cells on X, 160 on Y (left), 192 cells on X, 320 on Y (right).

are imposed for both experiments. Symmetry boundary conditions are imposed on both sides ($x = 0$ and $x = 24$), using the mirror state technique. The CFL number is still 1/2.

As explained in part 4, the simple well-balanced Finite Volume scheme described herein is based on the 0-Riemann invariants connection at each interface of the mesh. Thus we will focus here on *steady* states. Figure 6 provides the time residual:

$$R^n(a) = \sum_{i=1,N} |a_i^{n+1} - a_i^n|\Omega_i/\Delta t$$

for any variable a (N denotes the total number of cells in the computational domain). We will examine more specifically entropies S_1 and S_2 which are two among the eleven Riemann invariants of the standing wave associated with the eigenvalue $\lambda_0(W)$.

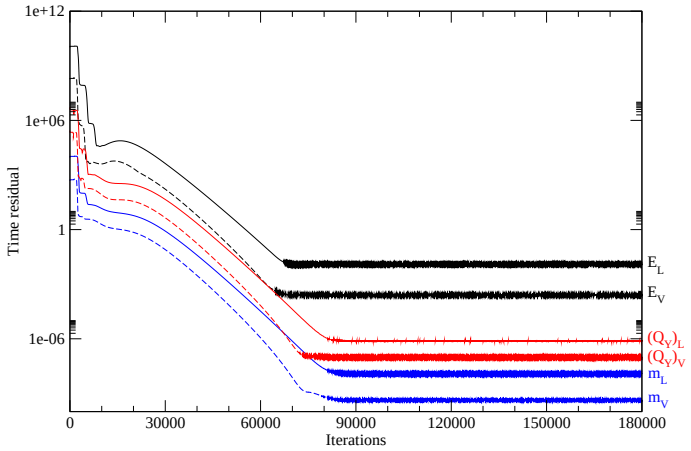

Figure 6: Test 3: Logarithm of time residual for energy, momentum and mass, for both phases, considering the finer mesh (d) (192x 320 cells). Subscript L corresponds to liquid and subscript V refers to vapour.

Figure 7 shows the liquid entropy profiles S_1 on different mesh sizes for the free approach, thus including real obstacles. Focusing on the porous approach, S_1 is constant and equal to 100000 in all the computational domain.

On Figure 8, entropy profiles for both phases have been plotted along the y-axis, for x situated in the middle of the domain ($x = 12$). Computations (a) to (d) have been performed on the real geometry including obstacles, and computation (e) has been performed with the porous approach. While entropy profiles are uniform with the porous approach, they are not constant with the free approach.

Figure 9 summarizes all liquid entropy profiles S_1 shown in Figure 8 on a same graph. The dashed black line corresponds to the porous approach on a coarse mesh, and plain lines correspond to the free approach. The brown one with crosses corresponds to the coarser mesh (a) presented on Figure 5, the blue one with stars to the second coarser mesh (b), the red one with circles to mesh (c), and the green one with triangles corresponds to the finer mesh (d) for the free approach.

Hence, both experiments obviously differ when focusing on entropy distributions. The present mesh refinement does not allow us to conclude definitely, but it seems very unlikely that the approximate solutions in the free approach would converge towards a uniform profile. It suggests that the mathematical tool provided by the well-balanced approach is fine, but that the current coupling conditions on the sharp free-porous interface, which enforce the preservation of all 0-Riemann invariants,

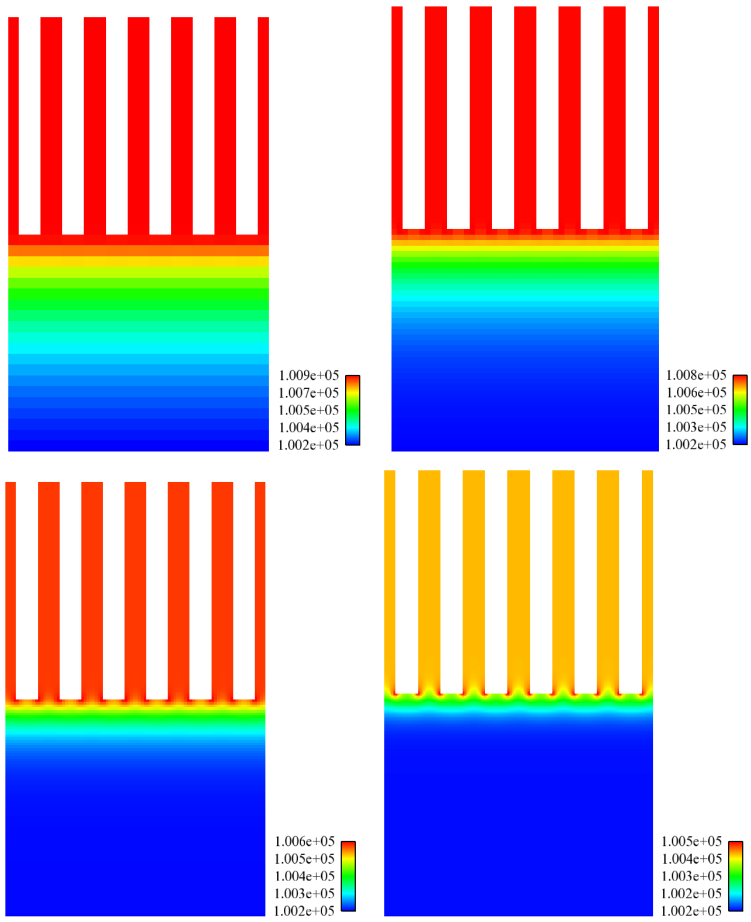

Figure 7: Test 3: Mean liquid entropy S_1 in a free medium with six obstacles, considering different meshes. Top : 24 cells on X, 40 on Y (left) , 48 cells on X, 80 on Y (right). Bottom: 96 cells on X, 160 on Y (left), 192 cells on X, 320 on Y (right).

must be improved from a physical point of view.

6.2.2 Test 4: Flow passing a region containing regular obstacles

We now focus on a domain which contains two medium transitions. First, we compute the free flow in a rectangular computational domain $[0, 24] \times [0, 30]$ containing six identical rectangular obstacles aligned with the y-direction in the middle of the domain (for $y \in [10, 20]$). Within this region, the fluid can flow through a surface, the aspect ratio of which is still $1/2$. A sketch is given in Figure 10 with different meshes.

In a second experiment, we consider again the porous approach. Thus, the computational domain is now the full rectangle $(x, y) \in [0, 24] \times [0, 30]$. The porosity distribution is given by $\epsilon(x, y) = 1$, while we prescribe $\epsilon(x, y) = 1/2$, for $y \in [10, 20]$.

[Free approach. Mesh size: 24 cells on X, 40 cells on Y]

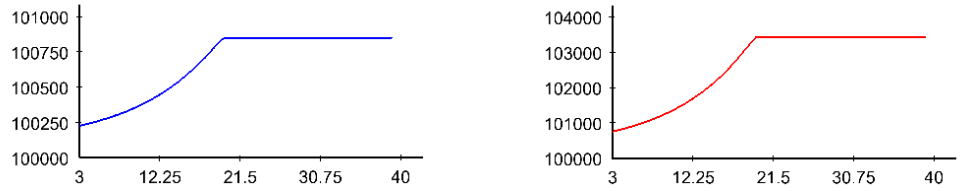

[Free approach. Mesh size: 48 cells on X, 80 cells on Y]

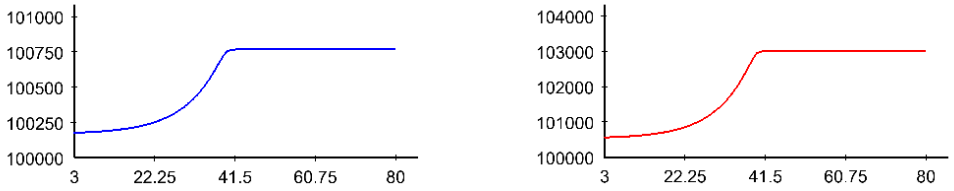

[Free approach. Mesh size: 96 cells on X, 160 cells on Y]

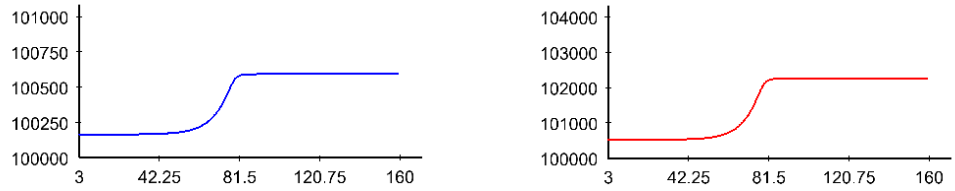

[Free approach. Mesh size: 192 cells on X, 320 cells on Y]

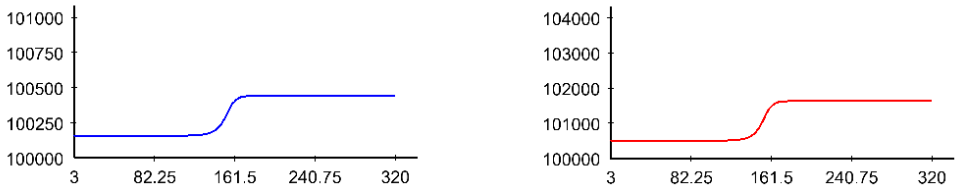

[Porous approach. Mesh size: 24 cells on X, 40 on Y]

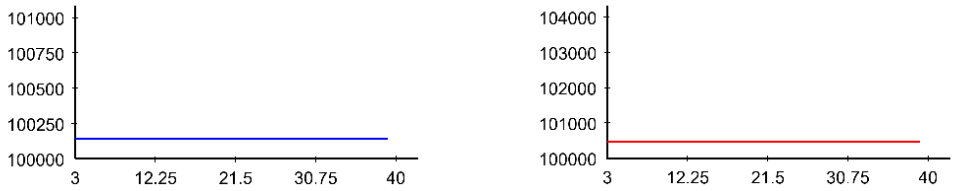

Figure 8: Test 3: Liquid and vapour entropy profiles S_1 (left) and S_2 (right) along the y-axis, for x situated in the middle of the domain. Computations (a) to (d) : free approach, computation (e) : porous approach. Values on the abscissa axis of the graphs correspond to the cell number in the y-direction.

Two meshes have been used here. The first one corresponds to the coarser mesh (a) of the figure 10 (24 cells on X, 30 on Y), and the second one corresponds to the finer mesh (d) (192 cells on X, 240 on Y) without obstacles.

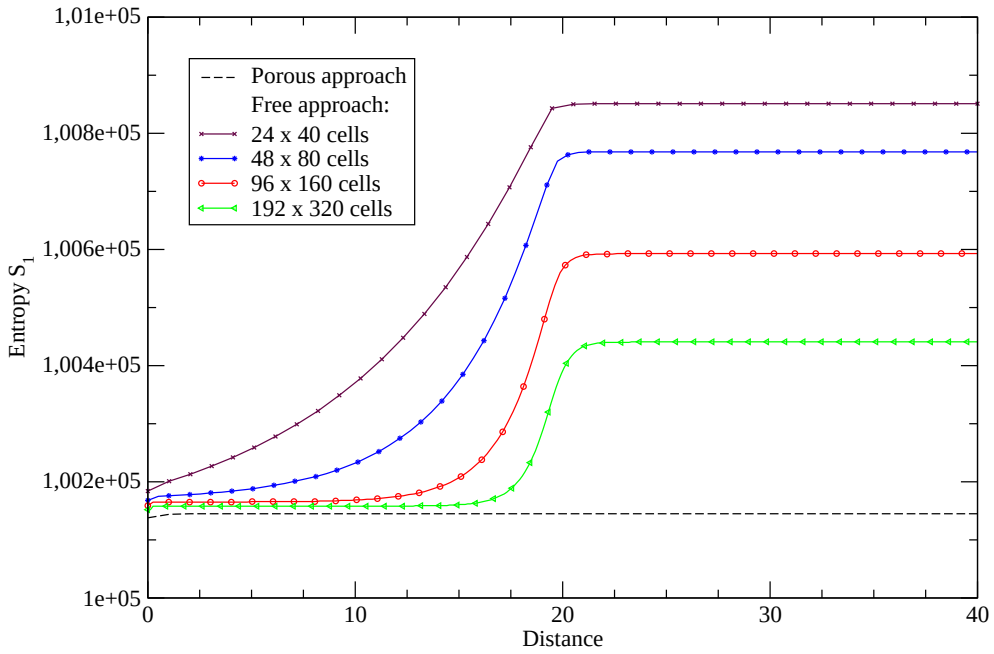

Figure 9: Test 3: Liquid entropy profiles S_1 for the porous approach (dashed black line) and the free approach (plain brown, blue, red, green lines correspond to coarse to fine mesh respectively).

The same inlet (for $y = 0$) and outlet (for $y = 30$) boundary conditions are imposed for both experiments, and these are the same as for test 3. Symmetry conditions are enforced on both sides of the computational domain ($x = 0$ and $x = 24$). The CFL number is still 1/2. We focus again on steady results (see Figure 11 for time residual) and we expect results that are similar to those obtained in test 3. The objective here is to make sure that discrepancies still remain, whenever the flow is incoming or outcoming the region including obstacles.

We still focus on entropy profiles. Figure 12 presents on the same graph the liquid entropy S_1 along the y-axis for $x = 12$, for both the free and porous approaches, when using different meshes. The dashed black line corresponds to the porous approach (coarse and fine meshes give the same result: S_1 is constant), and plain lines correspond to the free approach. Turning then to the free approach, the brown line with crosses corresponds to the coarser mesh (a), the blue one with stars to the second coarser mesh (b), the red one with circles to mesh (c), and the green one with triangles corresponds to the finer mesh (d).

We can once more observe on Figure 12 that each transition (free medium to

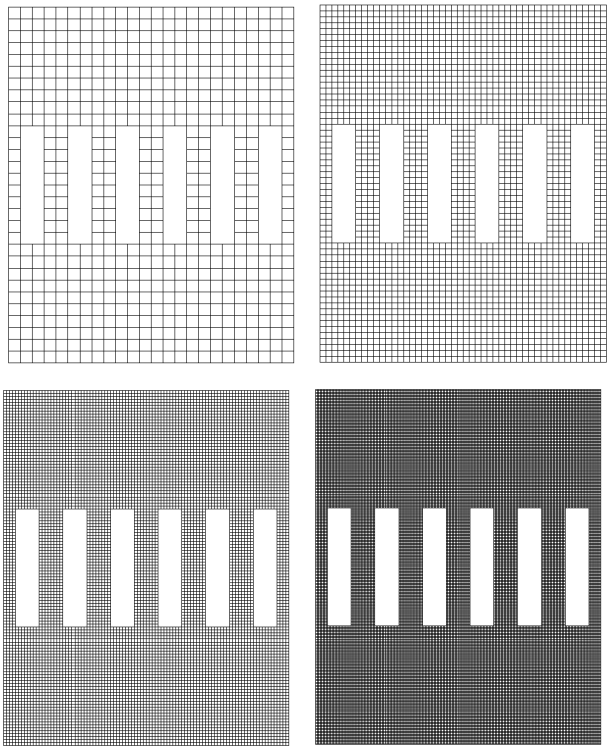

Figure 10: Computational domains used for the free approach with six identical rectangular obstacles in Test 4 (two medium changes). Top : 24 cells on X, 30 on Y (left) , 48 cells on X, 60 on Y (right). Bottom: 96 cells on X, 120 on Y (left), 192 cells on X, 240 on Y (right).

porous medium at $y = 10$, or the reverse at $y = 20$) leads to an increase of the entropy S_1 when focusing on the true approach with real obstacles, while the porous approach keeps the entropy constant.

6.3 On the influence of the number of obstacles

We now focus on the influence of the number of obstacles in the free approach. The main goal here is to make a comparison between different distributions of obstacles, while assuming a given aspect ratio 1/2. We will also recall the comparison with the porous approach. This will help to evaluate the validity of the porous formulation.

6.3.1 Presentation of Test 5

Thus we compute again the free flow in the same computational domain as for Test 4 ($(x, y) \in [0, 24] \times [0, 30]$) with 192 cells on X and 240 cells on Y, while choosing a different number of obstacles in the porous region. The given aspect ratio is still 1/2 in the middle of the domain (for $y \in [10, 20]$), that includes either 6, 12, 24 or 48 obstacles, when considering the free approach. A sketch is given in Figure 13.

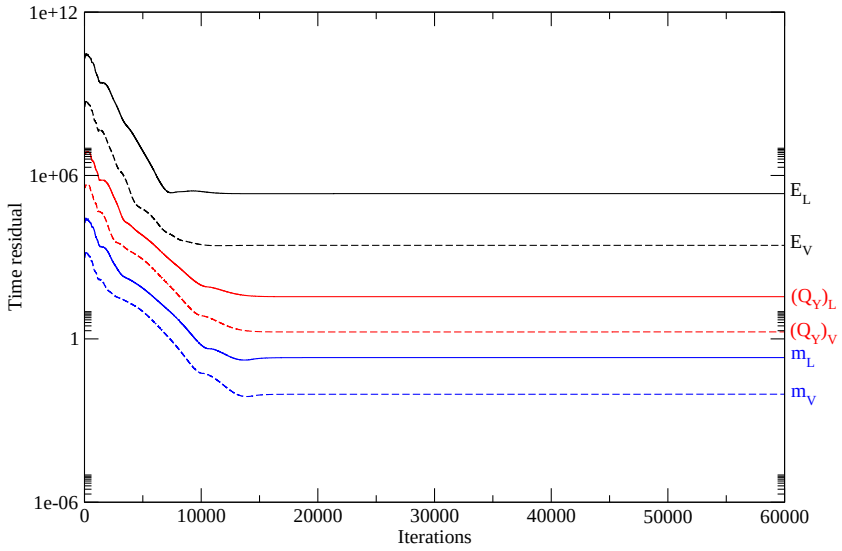

Figure 11: Test 4: Logarithm of the time residual of energy, momentum and mass for both phases for the finer mesh (d) (192x240 cells). Subscript L corresponds to the liquid and subscript V refers to the vapour.

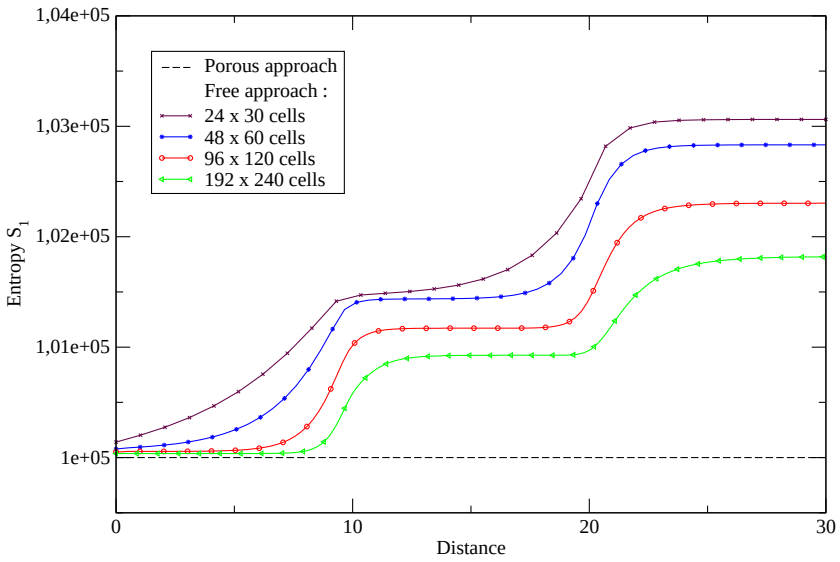

Figure 12: Liquid entropy profiles S_1 for the porous approach (dashed black line) and the free approach (plain lines) for Test 4 (including two medium changes).

In order to study the results obtained with the porous approach, the porosity distribution is again given by $\epsilon(x, y) = 1$ everywhere in the domain except for

$y \in [10, 20]$ where $\epsilon(x, y) = 1/2$.

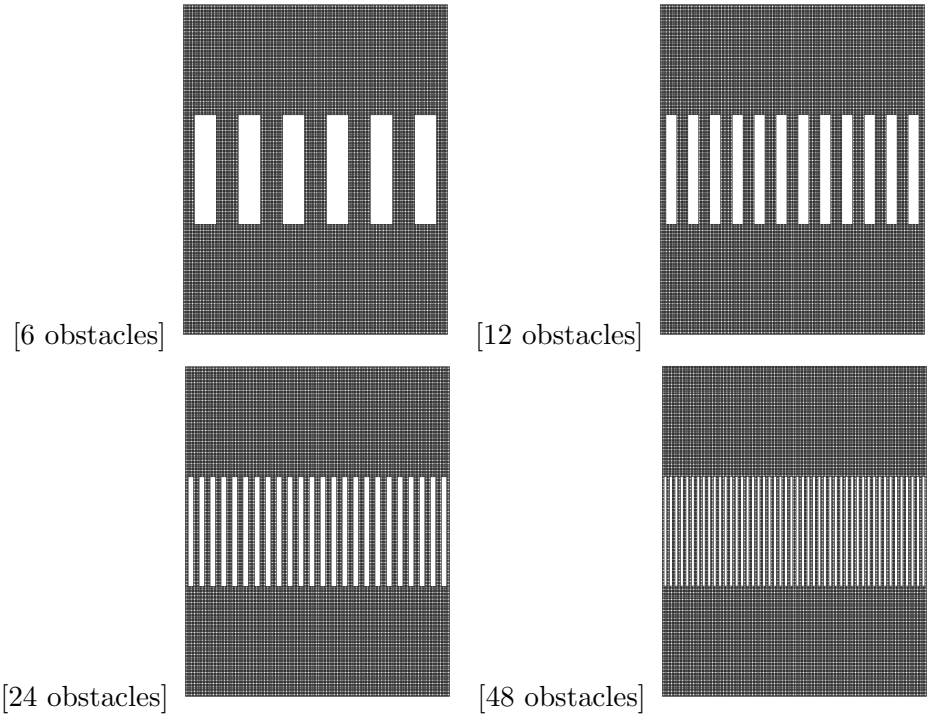

Figure 13: Computational domains used in Test 5 (192 cells on X, 240 on Y)

The same boundary conditions are imposed for both experiments (the same as for tests 3 and 4), and the CFL number is still 1/2.

We examine steady results, focusing on the Riemann invariants of the standing wave.

6.3.2 Entropy profiles for Test 5

Figure 14 presents the liquid entropy profiles S_1 along the y -axis for $x = 12$. The dashed black line corresponds to the porous approach and plain lines correspond to the free approach with different numbers of obstacles. The green (respectively red, blue, brown) line corresponds to the simulation of the free approach including 6 (respectively 12, 24, 48) obstacles, computed with a mesh including (192×240) cells.

Whatever the number of obstacles is, the free approach leads to an increase of the liquid entropy S_1 at each medium transition, but the results obviously differ, depending on the number of obstacles. The following table presents liquid entropy values for $y = 15$ (in the porous medium) and $y = 26, 25$ (in the free medium, output). The relative error between the constant state of each computation in the free medium - on the finer mesh- and the S_1's value for the porous approach are

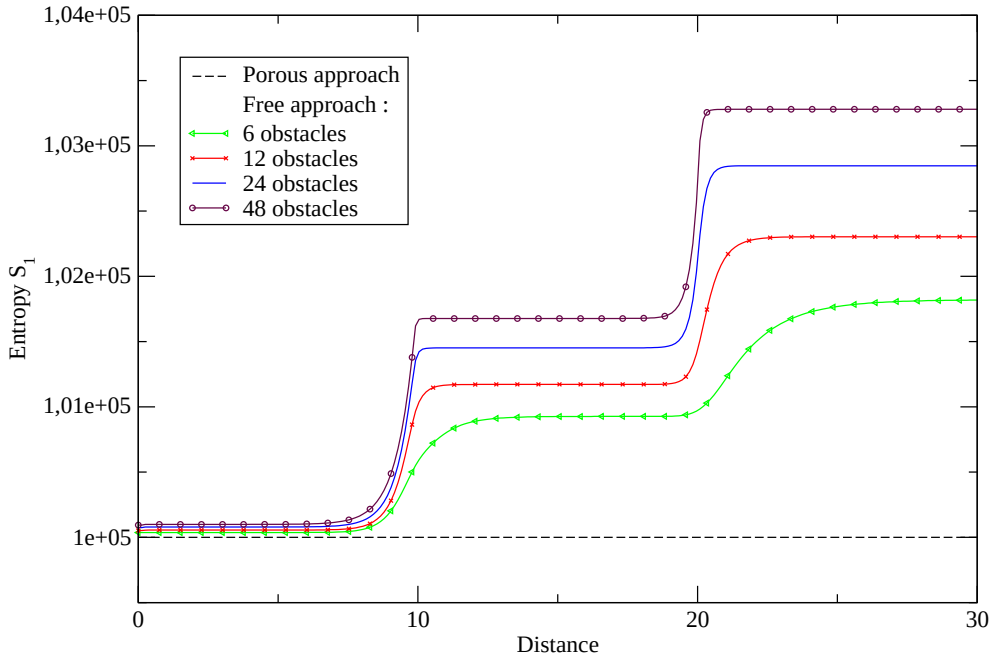

Figure 14: Liquid entropy profiles S_1 for the porous approach (dashed black line) and the free approach (plain lines) along the y-axis, using $6, 12, 24, 48$ obstacles. Mesh size: 192 x 240 cells

evaluated as follows :

$$\Delta_{S_1} = \left(\frac{(S_1(y))_{free} - (S_1(y))_{porous}}{(S_1(y))_{porous}} \right)$$

Approach	porous medium $y = 15$	fluid medium, output $y = 26,25$
Porous	$S_1 = 100000$	
Free - 6 obstacles	$S_1 = 100926$; $\Delta_{S_1} = 0,92\%$	$S_1 = 101816$; $\Delta_{S_1} = 1,82\%$
Free - 12 obstacles	$S_1 = 101172$; $\Delta_{S_1} = 1,17\%$	$S_1 = 102303$; $\Delta_{S_1} = 2,30\%$
Free - 24 obstacles	$S_1 = 101452$; $\Delta_{S_1} = 1,45\%$	$S_1 = 102847$; $\Delta_{S_1} = 2,84\%$
Free - 48 obstacles	$S_1 = 101677$; $\Delta_{S_1} = 1,67\%$	$S_1 = 103280$; $\Delta_{S_1} = 3,28\%$

On the basis of graph 14, computational results show that the associated error is less than 3%, and we also know from Test 4 results, that the error decreases with a mesh refinement. It also clearly arises that discrepancies slightly increase with the number of obstacles, for a given number of cells in the computational domain. However, it must be emphasized that a larger mesh refinement is expected in order to reach a fair level of accuracy, for the case involving the greater number of obstacles.

6.3.3 Test 5: Mass flow rate profiles

In order to compare the porous approach results where the mass flow rates are $(Q_k)_{por} = \epsilon m_k U_k.n$ on the one hand, and the free approach results where the mass

flow rates are $(Q_k)_{free} = m_k U_k.n$ on the other hand (since $\epsilon = 1$ everywhere), we focus on the mass flow rate integral over the x-axis, normal to the main flow direction. Thus the concept of the porous surface ϵ (equal to $1/2$ where $y \in [10, 20]$) may be taken into account in both the free and the porous approaches.

Focusing on *steady* results, we recall that the mass flow rate Q_k is a Riemann invariant in the standing wave for the porous approach. Turning then to the free approach, we note that the integral of the mass flow rate also has to be constant for steady states. This is true for *interface values for any mesh size*, and also for *cell mean values when the mesh size tends towards* 0 .

The discrete form of this integral $\int_x \alpha_k \rho_k U_k.n \, dS$, for a given $y \in [0, 30]$, is $\sum_i (\alpha_k \rho_k U_k.n)_i S_i$ along the corresponding line indexed by j. The discrete integral of the liquid mass flow rate is plotted on Figure 15, for all meshes, when the domain contains six obstacles. We emphasize here that *the integral that has been computed takes cell values into account.*

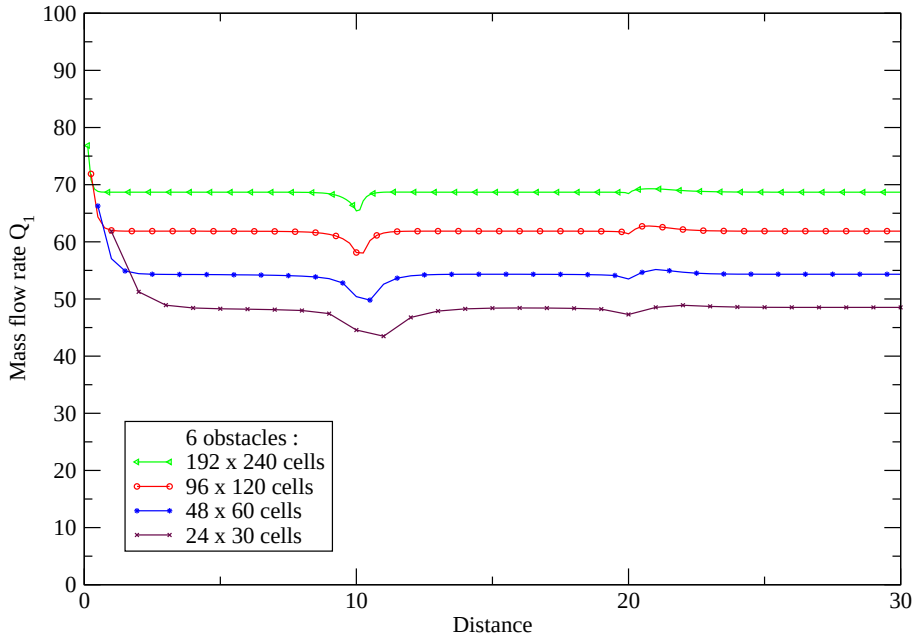

Figure 15: Discrete mass flow rate profiles Q_1 for the free approach (plain lines) along the y-axis (240 cells), focusing on Test5 including six obstacles, and for different mesh sizes.

We turn now to the influence of obstacles (see Figure 16). The dashed black line corresponds to the porous approach and plain lines correspond to the free approach. The green (respectively red, blue, brown) line corresponds to the simulation of the free approach including 6 (respectively 12, 24, 48) obstacles.

We notice that the integral mass flow rate is almost uniform around sharp tran-

sitions, whatever the mesh refinement is (see Figure 15), and also independently of the number of obstacles (see Figure 16). This is indeed confirmed by a mesh refinement. It confirms that the current coupling condition in the porous model, which enforces a constant mass flow rate on the sharp free-porous interface, is fine.

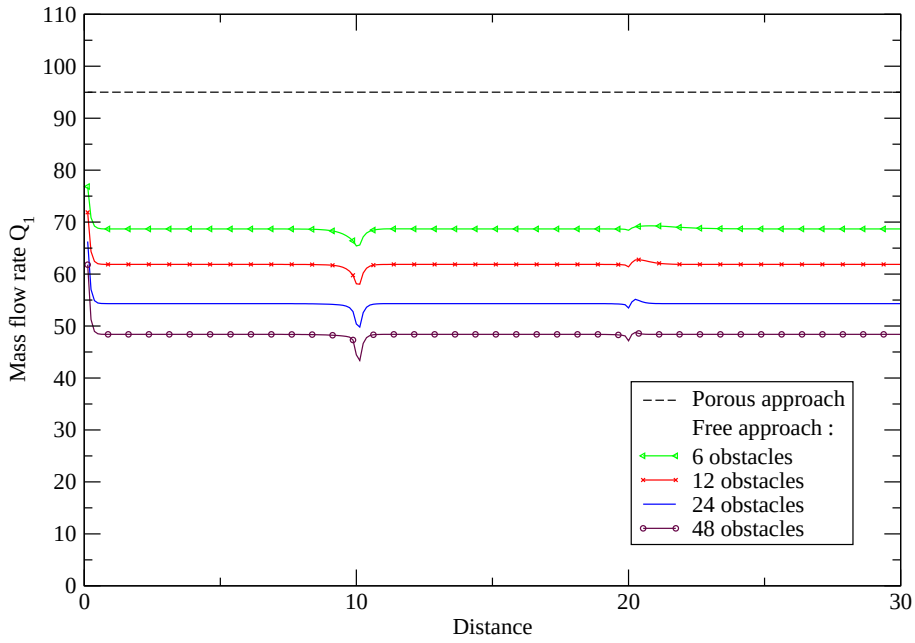

Figure 16: Profiles for liquid mass flow rates Q_1 for the porous approach (dashed black line) and the free approach (plain lines) along the y-axis (240 cells), considering $6, 12, 24, 48$ obstacles.

Similar results and comments pertaining to the third Riemann invariant of the standing wave (corresponding to the enthalpy H_k) hold. This again validates the basic porous approach in presence of a sharp free-porous transitions.

The last series of figures provides some velocity profiles.

7 Conclusion

One first main conclusion is that the simple well-balanced scheme described here is indeed a useful tool in order to tackle the computation of two-phase flows in domains containing porous areas. This is really interesting, since it suggests that one can now concentrate on the "ultimate" formulation for the coupling boundary conditions between a free and a porous region, and then rely on the proposed well-balanced numerical strategy in order to compute approximations of solutions that will comply with these prescribed -and enforced- boundary conditions.

Moreover, we have investigated and compared in this paper the results obtained while retaining the 3D homogeneized approach (the so-called porous formulation),

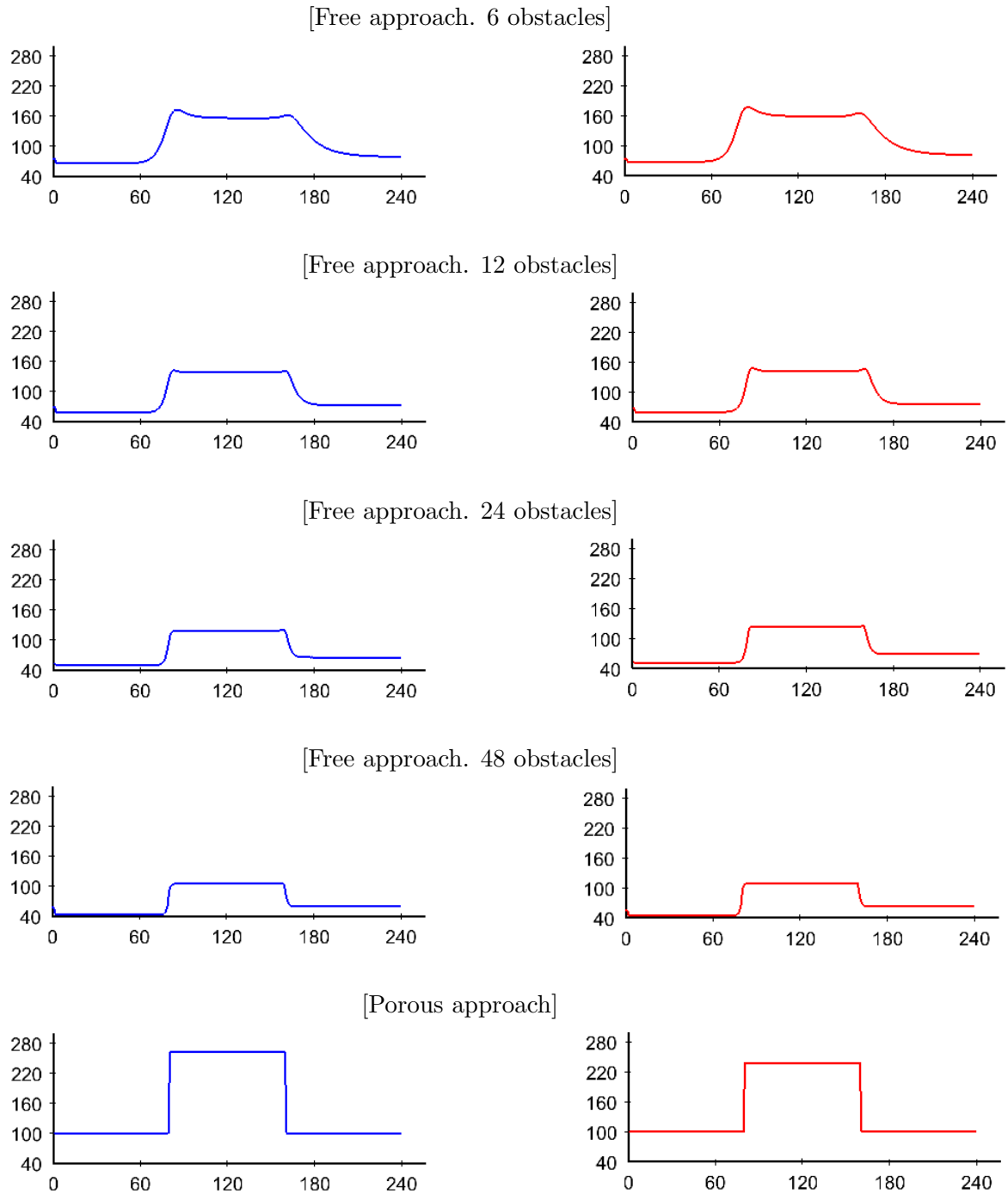

Figure 17: Liquid and vapour velocity profiles V_1 (on the left side) and V_2 (on the right side) along the y-axis, for x situated in the middle of the domain. Computations (a) to (d) : free approach, computation (e) : porous approach. Values on the abscissa axis of the graph correspond to the cell number.

or alternatively the true three-dimensional approach where all obstacles are taken into account in the computational domain and meshes. More precisely, we have examined discrepancies in results connected to the flow coming from a free region and entering a domain filled with tubes or rods aligned with the mean flow direction. This corresponds to a schematic representation of the flow entering the core region or a steam generator, in the coolant circuit of a pressurized water reactor. The comparison suggests a few conclusions that are listed below.

- *Concerning competitiveness*, we may claim that for a given number of cells, the porous approach enables to reach convergence (with respect to the mesh size) much faster than the true 3D approach. This of course is interesting for industrial purposes.
- *Concerning the suitablity of algorithms*, the proposed well-balanced scheme behaves well in the 3D porous approach, in terms of stability. Obviously its Rusanov flavour does not favour the accuracy, for a given mesh size, and one may expect that more accurate well-balanced approximate Riemann solvers (such as the one described in [14, 15]) might improve the accuracy of computations.
- *Turning then to the coupling boundary conditions*, the comparison suggests that the enforced coupling conditions through a free/porous interface that are implicitely provided by the Greenberg-Leroux formalism might be improved, and more precisely that the preservation of the entropy is a bit too rough. Some alternative proposals in that direction are currently investigated, which aim at providing realistic corrections such as those described in [18] .

Acknowledgments:

This work has been achieved in the framework of the NEPTUNE project, financially supported by CEA (Commissariat à l'Energie Atomique), EDF, IRSN (Institut de Radioprotection et de Sureté Nucléaire) and AREVA-NP. Part of the financial support of the first author is provided by ANRT (Association Nationale de la Recherche Technique, Ministère chargé de la recherche) through a EDF/CIFRE contract, and also by FSE (Fonds Social Européen). Both reviewers are also acknowledged for their remarks and suggestions which helped improving the initial manuscript.

8 Appendix A

We give below some details of the proof for property 5, that ensures the positivity of partial masses and void fractions if some CFL condition holds.

Partial masses
The proof is easy to obtain. Starting from the cell scheme (18):

$$\Omega_i(Z_i^{n+1} - Z_i^n) + \Delta t^n \sum_{j \in V(i)} \Big(F(Z_i^n, Z_{ij,i}^n, n_{ij}) S_{ij} \Big) + \Delta t^n (NCT)_i^n = 0 \qquad (26)$$

we know that cell values of partial masses are updated through:

$$\Omega_i((m_k)_i^{n+1} - (m_k)_i^n)... \\ +\frac{\Delta t^n}{2} \sum_{j\in V(i)} \Big((m_k U_k)_i^n . n_{ij} + (m_k U_k)_{ij,i}^n . n_{ij} - (r_{WB})_{ij}^n ((m_k)_{ij,i}^n - (m_k)_i^n) \Big) S_{ij} = 0 \tag{27}$$

Thus:

$$\Omega_i((m_k)_i^{n+1} - (m_k)_i^n) + \frac{\Delta t^n}{2} \sum_{j\in V(i)} \Big((m_k U_k)_{ij,i}^n . n_{ij} - (r_{WB})_{ij}^n ((m_k)_{ij,i}^n - (m_k)_i^n) \Big) S_{ij} = 0 \tag{28}$$

since $\sum_{j\in V(i)} n_{ij} S_{ij} = 0$. Hence we get:

$$\Omega_i (m_k)_i^{n+1} = ... \\ (m_k)_i^n \left(\Omega_i - \frac{\Delta t^n}{2} \sum_{j\in V(i)} (r_{WB})_{ij}^n S_{ij} \right) + \frac{\Delta t^n}{2} \sum_{j\in V(i)} (m_k)_{ij,i}^n \Big((r_{WB})_{ij}^n - (U_k)_{ij,i}^n . n_{ij} \Big) S_{ij} \tag{29}$$

Owing to the definition of $(r_{WB})_{ij}^n$, and to the fact that $0 \leq (m_k)_i^n$ and $0 \leq (m_k)_{ij,i}^n$, we may conclude that $(m_k)_i^{n+1}$ is positive provided that the following CFL-like condition holds:

$$\frac{\Delta t^n}{2\Omega_i} \sum_{j\in V(i)} (r_{WB})_{ij}^n S_{ij} \leq 1$$

which concludes the proof.

Void fractions

Once again, starting from (18), we know that cell values of void fractions are governed by:

$$\Omega_i((\alpha_2)_i^{n+1} - (\alpha_2)_i^n)... \\ +\Delta t^n (V_I)_i^n . \sum_{j\in V(i)} (\overline{\alpha}_2)_{ij} n_{ij} S_{ij} - \frac{\Delta t^n}{2} \sum_{j\in V(i)} (r_{WB})_{ij}^n \Big((\alpha_2)_{ij,i}^n - (\alpha_2)_i^n \Big) S_{ij} = 0 \tag{30}$$

Thanks to $(\alpha_2)_{ij,i}^n = (\alpha_2)_j^n$, we deduce:

$$\Omega_i (\alpha_2)_i^{n+1} = ... \\ (\alpha_2)_i^n \left(\Omega_i - \frac{\Delta t^n}{2} \sum_{j\in V(i)} (r_{WB})_{ij}^n S_{ij} \right) + \frac{\Delta t^n}{2} \sum_{j\in V(i)} (\alpha_2)_j^n \Big((r_{WB})_{ij}^n - (V_I)_i^n . n_{ij} \Big) S_{ij} \tag{31}$$

The definition of $(r_{WB})_{ij}^n$ and the above mentionned CFL condition enable to conclude that $(\alpha_2)_i^{n+1}$ remains positive, since all quantities $(\alpha_2)_m^n$ are assumed to be positive. A similar result holds for α_1.

9 Appendix B

Friction effects may be taken into account within the porous medium. For that purpose, we need to introduce additional terms f_k, g_k in both momentum and energy governing equations. These turn out to be :

$$\left\{\begin{array}{l} \partial_t(\epsilon) = 0 \\ \partial_t(\alpha_2) + V_I \cdot \nabla(\alpha_2) = \phi_2(W) \\ \partial_t(\epsilon m_k) + \nabla \cdot (\epsilon m_k U_k) = 0 \\ \partial_t(\epsilon m_k U_k) + \nabla \cdot (\epsilon m_k U_k \otimes U_k) + \epsilon \alpha_k \nabla(P_k) + \epsilon(P_k - P_I)\nabla(\alpha_k) = \epsilon D_k(W) + \epsilon f_k(W) \\ \partial_t(\epsilon \alpha_k E_k) + \nabla \cdot (\epsilon \alpha_k U_k (E_k + P_k)) + \epsilon P_I \partial_t(\alpha_k) = \epsilon \psi_k + \epsilon V_I \cdot D_k(W) + \epsilon g_k(W) \ . \end{array}\right. \tag{32}$$

We now wonder what is the influence of these friction terms on the entropy inequality. The derivation of the entropy time variation is straightforward. We thus only recall here the final expression:

$$\partial_t(\eta) + \nabla.(f_\eta) = S_\eta(W) + \epsilon \sum_k a_k(g_k(W) - f_k(W).U_k) \ . \tag{33}$$

Starting from expressions arising from the literature [3] , we get $g_k(W) = 0$ and:

$$f_k(W) = -M_k U_k \ . \tag{34}$$

Obviously, the friction effects will contribute to the entropy production provided that the matrices $M_k + M_k^t$ are positive half-definite, which is guaranteed by standard closure laws (see [3]).

10 Appendix C

Jump conditions in single GNL waves are simply those corresponding to a pure single phase framework, due to the decoupling of both phases on each side of the coupling wave associated to λ_1. In a one-dimensional framework, an unsteady shock wave, separating two states W_l, W_r, and travelling at speed σ in the n direction is characterized by :

$$\begin{array}{c} [\alpha_k]_l^r = 0 \\ -\sigma[\rho_k]_l^r + [\rho_k U_k]_l^r = 0 \\ -\sigma[\rho_k U_k]_l^r + [\rho_k U_k^2 + P_k]_l^r = 0 \\ -\sigma[E_k]_l^r + [U_k(E_k + P_k)]_l^r = 0 \end{array} \tag{35}$$

11 Appendix D

We assume that both ϵ_i and ϵ_j are non zero. On the ij interface separating cells i and j (on the left side and right side respectively), we introduce the outward unit normal n_{ij}. We also define vectors $(\tau_1)_{ij}$ and $(\tau_2)_{ij}$ in such a way that $(n, \tau_1, \tau_2)_{ij}$ is an orthonormal basis. $Z_{ij,i}$ must comply with :

$$Inv_m^0(Z_{ij,i}^n, \epsilon_i) = Inv_m^0(Z_j^n, \epsilon_j)$$

for $m = 0, .., 10$. Thus we get:

$$(\alpha_2)^n_{ij,i} = (\alpha_2)^n_j$$

$$(s_k)^n_{ij,i} = (s_k)^n_j$$

$$(U_k)^n_{ij,i} \cdot (\tau_1)_{ij} = (U_k)^n_j \cdot (\tau_1)_{ij}$$

$$(U_k)^n_{ij,i} \cdot (\tau_2)_{ij} = (U_k)^n_j \cdot (\tau_2)_{ij}$$

and:

$$\epsilon_i(\alpha_k)^n_{ij,i}(\rho_k)^n_{ij,i}(U_k)^n_{ij,i} \cdot n_{ij} = \epsilon_j(\alpha_k)^n_j(\rho_k)^n_j(U_k)^n_j \cdot n_{ij}$$

$$h_k((s_k)^n_{ij,i}, (\rho_k)^n_{ij,i}) + 1/2((U_k)^n_{ij,i} \cdot n_{ij})^2 = h_k((s_k)^n_j, (\rho_k)^n_j) + 1/2((U_k)^n_j \cdot n_{ij})^2$$

where : $h_k(s_k, \rho_k) = e_k(P_k(s_k, \rho_k), \rho_k) + P_k(s_k, \rho_k)/\rho_k$. Setting $X = (\rho_k)^n_{ij,i}$, we must solve :

$$\psi^n_{ij,i}(X) = 0 \tag{36}$$

where :

$$\psi^n_{ij,i}(X) \stackrel{def}{=} \left(h_k((s_k)^n_j, X) - h_k((s_k)^n_j, (\rho_k)^n_j)\right) + 1/2((U_k)^n_j \cdot n_{ij})^2 \left(\frac{(\epsilon_j(\rho_k)^n_j)^2}{(\epsilon_i X)^2} - 1\right) \tag{37}$$

The solution is obviously $X = (\rho_k)^n_j$ when $\epsilon_i = \epsilon_j$. If $\epsilon_i \neq \epsilon_j$, we use the following procedure :

- If $(U_k)^n_j \cdot n_{ij} = 0$, the solution of (36) is $X = (\rho_k)^n_j$.
- Otherwise, we compute $X_{min} > 0$ solution of :

$$X^3_{min}\left(\partial_{\rho_k}\left(h_k(s_k, \rho_k)\right)\right)((s_k)^n_j, X_{min}) = \left(\frac{\epsilon_j(\rho_k)^n_j(U_k)^n_j \cdot n_{ij}}{\epsilon_i}\right)^2 > 0 \tag{38}$$

  Then:

  - Either:

$$\psi^n_{ij,i}(X_{min}) \leq 0$$

    In that case, the equation (36) admits two solutions $X^- \in]0, X_{min}]$ and $X^+ \in [X_{min}, +\infty[$. The final solution is $X = X^-$ if $(\rho_k)^n_j \leq X_{min}$, and $X = X^+$ if $X_{min} \leq (\rho_k)^n_j$.
  - Otherwise, (36) has no solution. We enforce in that case : $X = X_{min}$, thus minimizing $(\psi^n_{ij,i}(X))^2$.

12 Bibliography

References

[1] Ambroso A., Chalons C. , Coquel F., Galié T., "Relaxation and numerical approximation of a two-fluid two-pressure diphasic model", *Math. Model. Numer. Analysis*, vol. 43, pp. 1063–1097, 2009.

[2] Ambroso A., Chalons C. , Coquel F., Godlewski E., Lagoutière F., Raviart P. A., Seguin N., Working group on the interfacial coupling of models, http://www.ann.jussieu.fr/groupes/cea.

[3] Aubry S., Cahouet J., Lequesne P., Nicolas G., Pastorini S., "THYC: Code de Thermohydraulique des Coeurs de Réacteurs. Version 1 .0 Modélisation et Méthodes Numériques", *Rapport EDF H-T10-1988-02769-FR*, in French, 1988.

[4] Baer M.R., Nunziato J.W., "A two-phase mixture theory for the deflagration to detonation transition (DDT) in reactive granular materials", *Int. J. Multiphase Flow*, vol. 12(6), pp. 861–889, 1986.

[5] Bouchut F., "Nonlinear stability of Finite Volume methods for hyperbolic conservation laws, and well-balanced schemes for sources", *Frontiers in Mathematics series, Birkhauser*, 2004.

[6] Z. Chen and R. Ewing, "Comparison of various formulations of three-phase flow in porous media", *J. of Comp. Phys.*, vol. 132, pp 362–373, 1997.

[7] Coquel F., Gallouët T., Hérard J.M., Seguin N., "Closure laws for a two-fluid two-pressure model", *C. R. Acad. Sci. Paris*, vol. I-332, pp. 927–932, 2002.

[8] Gallouët T., Helluy P., Hérard J.-M., Nussbaum J., "Hyperbolic relaxation model for granular flow", *Math. Model. Numer. Analysis*, vol. 44, pp. 371-400, 2010.

[9] Gallouët T., Hérard J.-M., Seguin N., "Numerical modelling of two phase flows using the two-fluid two-pressure approach", *Math. Mod. Meth. in Appl. Sci.*, vol. 14(5), pp. 663-700, 2004.

[10] Girault L., Hérard J.-M., "A two-fluid hyperbolic model in a porous medium", *Math. Model. Numer. Analysis*, 2010.

[11] Godlewski E., "Coupling fluid models. Exploring some features of interfacial coupling", *Proceedings of Finite Volumes for Complex Applications V, ISTE-Wiley*, pp. 87-102, Aussois, France, June 8-13, 2008.

[12] Greenberg J.M., Leroux A.Y., "A well balanced scheme for the numerical processing of source terms in hyperbolic equations", *SIAM J. Num. Anal.*, vol. 33(1), pp. 1–16, 1996.

[13] Guillemaud V., "Modélisation et simulation numérique des écoulements diphasiques par une approche bifluide à deux pressions", *P*hD thesis, Université Aix Marseille I, Marseille, France, 27th of March, 2007.

[14] Helluy P., Hérard J.M., Mathis H., *A* well-balanced approximate Riemann solver for variable cross-section compressible flows, AIAA paper 2009-3540, see: http://www.aiaa.org/, 2009.

[15] Hérard J.M. , "A rough scheme to couple free and porous media", *Int. J. Finite Volumes (electronic)*, http://www.latp.univ-mrs.fr/IJFV/, vol. 3(2), pp. 1-28, 2006.

[16] Hérard J.-M., "Un modèle hyperbolique diphasique bi-fluide en milieu poreux", *CRAS Paris Mécanique*, vol. 336, pp. 650-655, 2008.

[17] Hérard J.-M., Hurisse O., "Couplage interfacial d'un modèle homogène et d'un modèle bifluide", *internal EDF report H-I81-2006-04691-FR*, in French, 2006.

[18] Idel'cik I., "Mémento des pertes de charges", *Collection de la Direction des Etudes et Recherches d'Electricité de France*, in French, Eyrolles, pp. 1-504, 1986.

[19] Kapila A.K., Son S.F., Bdzil J.B., Menikoff R., Stewart D.S., "Two-phase modeling of a DDT: structure of the velocity relaxation zone", *Phys. of Fluids*, vol. 9(12), pp. 3885–3897, 1997.

[20] Kröner D., Le Floch P., Thanh M.D., "The minimum entropy principle for compressible fluid flows in a nozzle with discontinuous cross section", *Math. Mod. Num. Anal.* , vol. 42(3), pp. 425-443, 2008.

[21] Kröner D. , Thanh M.D., "Numerical solution to compressible flows in a nozzle with variable cross-section", *SIAM J. Numer. Anal.* , vol. 43(2), pp. 796–824, 2006.

[22] M. Valette and S. Jayanti, "Annular dispersed flow calculations with a two-phase three field model", *European Two phase Flow Group Meeting, Norway*, internal CEA report DTP/SMTH/LMDS/2003-085, 2003.